ACS APPLIED MATERIALS & INTERFACES

Research Article

www.acsami.org

α-NaYb(Mn)F_4:Er^{3+}/Tm^{3+}@$NaYF_4$ UCNPs as "Band-Shape" Luminescent Nanothermometers over a Wide Temperature Range

Xia Xu,[†,‡] Zhuo Wang,[†,‡] Pengpeng Lei,[†,‡] Yingning Yu,[†] Shuang Yao,[†] Shuyan Song,[†] Xiuling Liu,[†] Yue Su,[†,‡] Lile Dong,[†,‡] Jing Feng,*[,†] and Hongjie Zhang*[,†]

[†]State Key Laboratory of Rare Earth Resource Utilization, Changchun Institute of Applied Chemistry, Chinese Academy of Science, 5625 Renmin Street, Changchun, Jilin 130022, China

[‡]University of Chinese Academy of Sciences, Beijing 100049, China

Supporting Information

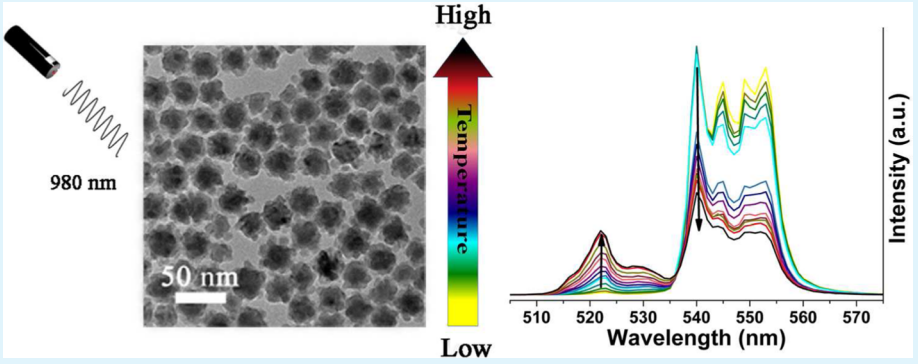

ABSTRACT: Novel flower-like α-NaYb(Mn)F_4:Er^{3+}/Tm^{3+}@$NaYF_4$ upconversion nanoparticles (UCNPs) as luminescent nanothermometers have been developed by combining liquid−solid solution hydrothermal strategy with thermal decomposition strategy. Under 980 nm excitation, they exhibit intense upconversion luminescence and temperature-dependent upconversion luminescence over a wide temperature range. The influence of temperature on "band-shape" upconversion luminescence (UCL) spectra and the intensity of emission bands are analyzed and discussed in detail. We further successfully test and verify that intensity ratios R_{Er} of $^2H_{11/2} \rightarrow {}^4I_{15/2}$ and $^4S_{3/2} \rightarrow {}^4I_{15/2}$ and R_{Tm} of $^1G_4 \rightarrow {}^3H_5$ and $^3H_4 \rightarrow {}^3H_6$ are sensitive to temperature, and the population of active ions follows Boltzmann-type population distribution very well. These luminescent nanothermometers could be applied over a wide temperature range from 123 to 423 K with high sensitivity, which enable them to be excellent candidates for temperature sensors.

KEYWORDS: *lanthanide, luminescent nanothermometer, upconversion nanoparticles, thermally coupled, band-shape, sensitivity*

1. INTRODUCTION

Temperature is one of the most fundamental parameters as it is a principal thermodynamic property.[1] Temperature measurement in different environments requires different sensitive thermometer performance.[2,3] Motivated by various fundamental and practical applications, many kinds of thermometry techniques have been elaborated.[4,5] Among these techniques for measuring temperature, luminescence-based thermometers attract much attention because of their fast response, high precision, and resolution.[6] Recently, QD-based,[7,8] dye-based,[9,10] and lanthanide-based[11−15] luminescence thermometers have been studied widely due to the relationship between luminescence properties and temperature. However, most of these luminescence thermometers suffer from the drawbacks of UV or short-wavelength visible excitation, which would cause background luminescence and Raman scattering, and hinder their applications in biological environment. Luminescent thermometers excited in the near-infrared (NIR) region are demanded to overcome these disadvantages.[16] Lanthanide-doped UCNPs are capable of converting low-energy radiation to high-energy through the two-photon or the multiphoton process. NIR excitation can significantly minimize background autoluminescence from the biological tissues, conquer photobleaching and phototoxicity, increase the penetration depth, and greatly improve the signal-to-noise ratio, resolution, and sensitivity in biological detection.[17] In addition, lanthanide-doped UCNPs are widely studied due to their attractive optical and chemical features, such as sharp absorption and emission lines, large Stoke's shifts, low toxicity, and superior photostability,[18,19] thus they have potential applications in displays,[20,21] solar cells,[22] biolables,[17,23,24] drug delivery,[25] photoactivation,[26] and so on.[27−31] Moreover, well-developed synthesis methods[32] and well-designed nanostructures[33] make it to prepare a wide range of nanoparticles with different phases,

Received: July 1, 2015
Accepted: August 27, 2015
Published: August 27, 2015

DOI: 10.1021/acsami.5b05876
ACS Appl. Mater. Interfaces 2015, 7, 20813−20819

morphologies, structures, and functions.[34−37] Now, lanthanide-doped UCNPs are regarded as a new generation of luminescent nanothermometers.[38]

As has been well established, the luminescence of lanthanide-doped UCNPs is strongly temperature-dependent, and the multiple emission bands are sensitive differently to temperature,[39,40] which enable them to be excellent candidates for temperature sensors. Capobianco et al.[41] reported a novel nanothermometer, which is based on the intensity ratio of the green emission bands of Er^{3+} ($^2H_{11/2} \rightarrow {}^4I_{15/2}$ and $^4S_{3/2} \rightarrow {}^4I_{15/2}$) changes with temperature, was used to obtain thermal profiles created when heating a colloidal solution of $NaYF_4$:Yb^{3+},Er^{3+} nanocrystals in water using a pump−probe experiment. CaF_2:Yb^{3+},Tm^{3+} UCNPs were reported by Adolfo Speghini et al.[42] as the nanothermometers, because the thermally coupled sub-Stark energy levels (790 and 800 nm) belonging to the $^3H_4$ excited state of Tm^{3+} are sensitive to temperature change. Similar results were observed in temperature-dependent luminescence of β-$NaYbF_4$:Tm^{3+}@SiO_2 core−shell microparticles, which confirm that the $^3F_2$ and $^3H_4$ are thermally coupled levels in the temperature range from 400 to 700 K.[43] Furthermore, temperature-dependent UCL properties of the nanoparticles with different sizes and crystalline phases were studied.[44,45] However, most of the temperature-dependent UCL properties were studied above 273 K, and the influence of temperature on thermally coupled levels of Er^{3+} and Tm^{3+} in a wide temperature range (above and below 273 K) has been reported rarely, which is worthy of being studied and discussed.

Herein, we synthesized novel flower-like α-NaYb(Mn)F_4@$NaYF_4$ UCNPs with the average diameter of 27 nm. Under 980 nm excitation, Er^{3+} and Tm^{3+} doped UCNPs exhibit intense upconversion luminescence. The main highlights of this work are the temperature-dependent UCL properties of Er^{3+} and Tm^{3+} doped α-NaYb(Mn)F_4@$NaYF_4$ UCNPs. The temperature has different influences on the different emission bands, and the thermally coupled levels of Er^{3+} ($^2H_{11/2}$ and $^4S_{3/2}$) and Tm^{3+} ($^1G_4$ and $^3H_4$) are discussed in a wide temperature range from 123 to 423 K. The results indicate that α-NaYb(Mn)F_4:Er^{3+}/Tm^{3+}@$NaYF_4$ UCNPs are excellent candidates for temperature sensors with high sensitivity.

2. EXPERIMENTAL SECTION

2.1. Materials. $LnCl_3{\cdot}6H_2O$ (99.99%, Ln = Yb, Y, Er, and Tm), Ln_2O_3 (99.99%, Ln = Gd, Y, and Lu), $Na(CF_3COO)$ (97%), CF_3COOH (99.0%), oleic acid (OA) (analytical grade), and 1-octadecene (ODE) (90%) were purchased from Aladdin Reagents. $MnCl_2{\cdot}4H_2O$ (analytical grade) was obtained from Xilong Chemical Co., Ltd. NaOH, NaF, ethanol, and cyclohexane were all analytical grade and obtained from Beijing Chemical Reagents. All the reagents and solvents were used as received without further purification. $Ln(CF_3COO)_3$ was prepared by dissolving the respective Ln_2O_3 in trifluoroacetic acid.

2.2. Synthesis of α-NaYb(Mn)F_4:Er^{3+}/Tm^{3+} UCNPs. Mn^{2+} ion-doped $NaYbF_4$:Er^{3+} UCNPs were prepared as reported previously.[46] A 2.6 mL mixed water solution of $YbCl_3$ (0.68 mmol), $MnCl_2$ (0.3 mmol), and $ErCl_3$ (0.02 mmol) was added dropwise to a mixture of NaOH (3 g), deionized water (1.5 mL), ethanol (10 mL), and oleic acid (5 mL) under stirring. Then, 4 mmol of NaF dissolved in 2 mL of deionized water was added dropwise to the mixture slowly. The mixture was stirred thoroughly for about 30 min to form a stable white emulsion-like mixture, and the colloidal solution was transferred into a 50 mL Teflon-lined autoclave, sealed, and heated at 200 °C for 8 h. When the system was cooled to room temperature naturally, the products were separated by centrifugation, washed with ethanol several times, and then redispersed in cyclohexane. For the synthesis of α-NaYb(Mn)F_4:Tm^{3+} nanocrystals, a molar ratio of Yb:Mn:Tm = 69.5:30:0.5 was adopted for the preparation following the same procedure.

2.3. Synthesis of α-NaYb(Mn)F_4:Er^{3+}/Tm^{3+}@$NaYF_4$ UCNPs. $Y(CF_3COO)_3$ was prepared according to the literature, dissolving the respective Y_2O_3 in trifluoroacetic acid.[47] The synthesis of α-NaYb(Mn)F_4:Er^{3+}/Tm^{3+}@$NaYF_4$ UCNPs was modified from the previous procedure.[48] In brief, 1 mmol of as-prepared α-NaYb(Mn)F_4:Er^{3+}/Tm^{3+} nanocrystals, 1 mmol of $Na(CF_3COO)$, and 1 mmol of $Y(CF_3COO)_3$ were taken as the precursors and added into a three-necked flask which contained the mixture of OA (6.5 mL) and ODE (6.5 mL) at room temperature. The mixture was then heated to 100 °C to remove oxygen and water with vigorous magnetic stirring under vacuum for 10 min in a temperature-controlled electromantle and then maintained at 100 °C for 0.5 h under an Ar atmosphere to form a transparent solution. The solution was then heated to 250 °C at a heating rate of 20 °C/min under Ar atmosphere, maintained at this temperature for 0.5 h, and then cooled to room temperature. The resulting nanoparticles were precipitated by addition of an excess amount of ethanol, collected by centrifugation, washed several times with ethanol, and finally dried in vacuum at 60 °C to obtain the dried powder.

2.4. Synthesis of α-NaYb(Mn)F_4@$NaGdF_4$ and α-NaYb(Mn)F_4@$NaLuF_4$ UCNPs. The synthetic procedure was the same as that used to synthesize α-NaYb(Mn)F_4@$NaYF_4$, except for using $Gd(CF_3COO)_3$ or $Lu(CF_3COO)_3$ instead of $Y(CF_3COO)_3$ at the initial stage.

2.5. Characterization. The powder X-ray diffraction (XRD) patterns were recorded on a Bruker D8 ADVANCE X-ray diffractometer using Cu Kα radiation (40 kV, 40 mA, λ = 0.15418 nm). The 2θ angle of the spectra was obtained at a scanning rate of 5°/min. The TEM and HRTEM images were performed using a FEI TECNAI G2 high-resolution transmission electron microscope operating at 200 kV. The temperature-dependent upconversion luminescence spectra of the power were measured with a steady state and time-resolved fluorescence spectrometers (FLSP-920) equipped with a 980 nm laser.

3. RESULTS AND DISCUSSION

3.1. Phase and Morphology. First, the composition and phase purity of α-NaYb(Mn)F_4 and α-NaYb(Mn)F_4@$NaYF_4$ UCNPs are investigated by X-ray powder diffraction (XRD). As shown in Figure 1, the XRD patterns of core and core−shell UCNPs can be indexed to pure cubic phase $NaYbF_4$ (JCPDS:77-2043) very well, and no trace of other phases or impurities are detected. The smaller Mn^{2+} ions instead of Yb^{3+} ions in $NaYbF_4$ host lattice could induce the transformation

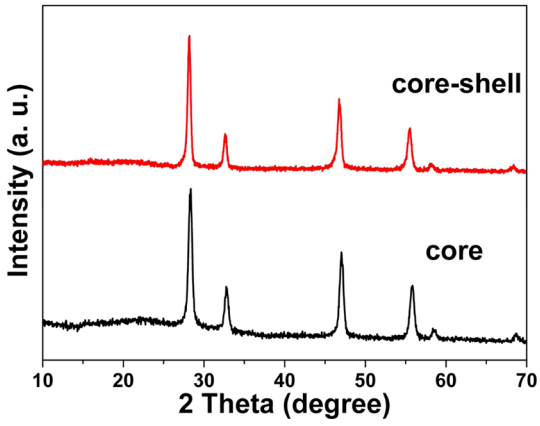

Figure 1. XRD patterns of α-NaYb(Mn)F_4 and α-NaYb(Mn)F_4@$NaYF_4$ UCNPs.

DOI: 10.1021/acsami.5b05876
ACS Appl. Mater. Interfaces 2015, 7, 20813−20819

from hexagonal to cubic phase. Finally, we have successfully obtained the cubic phase instead of the mixture of cubic and hexagonal phases (Figure S1, Supporting Information).

Figure 2 exhibits the transmission electron microscopy (TEM) images and size distributions of α-NaYb(Mn)F_4 and

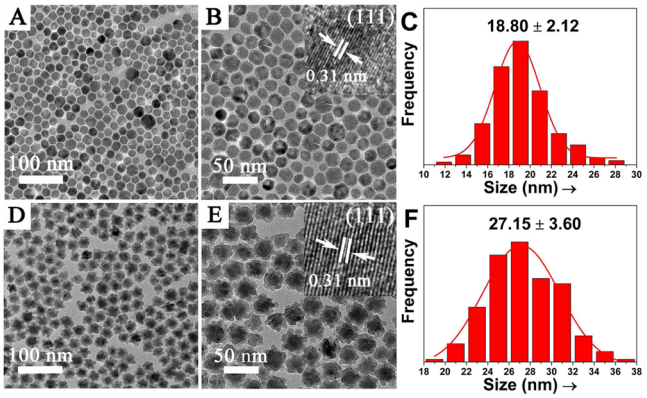

Figure 2. Low- (A), high-magnification (B) TEM images and size distribution (C) of α-NaYb(Mn)F_4 core UCNPs, low- (D), high-magnification (E) TEM images and size distribution (F) of α-NaYb(Mn)F_4@$NaYF_4$ core–shell UCNPs. Insets in (B and E) are the corresponding HRTEM images of α-NaYb(Mn)F_4 and α-NaYb(Mn)-F_4@$NaYF_4$ UCNPs.

α-NaYb(Mn)F_4@$NaYF_4$ UCNPs. As one can see, the synthesized α-NaYb(Mn)F_4 UCNPs by liquid–solid solution (LSS) hydrothermal strategy appear nearly spherical in shape and monodisperse (Figures 2A and 2B), and the average diameter of nanoparticles is around 18 nm (Figure 2C). After being coated with the shell layer via thermal decomposition of $Ln(CF_3COO)_3$ precursors, the as-synthesized α-NaYb(Mn)-F_4@$NaYF_4$ UCNPs look like uniform flowers (Figures 2D and 2E) with the average diameter of 27 nm (Figure 2F). In the high-resolution transmission electron microscopy (HRTEM) images, the lattice fringes on the individual nanocrystal are distinguished clearly, indicating that the prepared core and core–shell nanocrystals possess high crystallinity. The observed *d*-spacing of the lattice fringes in the insets of both Figures 2B and 2E are measured to be 0.31 nm, corresponding to the (111) plane of α-NaYb(Mn)F_4 and α-NaYb(Mn)F_4@$NaYF_4$ UCNPs, respectively. Both the interplanar distances coincide with the *d*-spacing for the (111) lattice planes of cubic $NaYbF_4$.

Out of curiosity for their flower-like morphology, we studied the impact of epitaxial growth with different ionic radius. Interestingly, the core–shell structure with a tensile strained shell looks compact, such as α-NaYb(Mn)F_4@$NaLuF_4$, as shown in Figure S2A, while the compressively strained shell looks incompact, such as α-NaYb(Mn)F_4@$NaGdF_4$ (Figure S2B).[49] In addition, whether the core looks spherical or cubed, the core–shell structure presents novel flower-like morphology in our system (Figure S3).

3.2. Upconversion Luminescence Properties. Under excitation with the 980 nm laser, the UCL spectra of α-NaYb(Mn)F_4:Er^{3+}@$NaYF_4$ and α-NaYb(Mn)F_4:Tm^{3+}@$NaYF_4$ nanoparticles are shown in Figure 3. The obtained α-NaYb(Mn)F_4:Er^{3+}@$NaYF_4$ UCNPs exhibit green emissions centered at 522 and 540 nm, which are assigned to $^2H_{11/2} \rightarrow {}^4I_{15/2}$ and $^4S_{3/2} \rightarrow {}^4I_{15/2}$ transitions of Er^{3+}, respectively, and the red emission centered at 652 nm corresponds to $^4F_{9/2} \rightarrow {}^4I_{15/2}$ transition of Er^{3+} (as shown in Figure 3A). The high red to

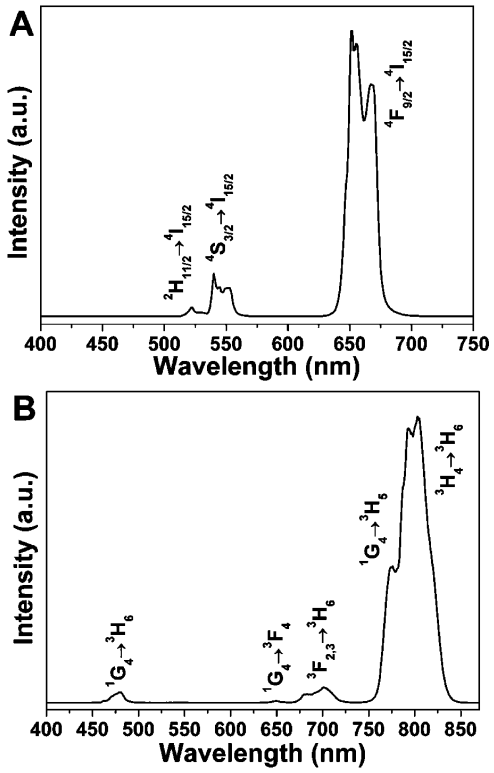

Figure 3. UCL spectra of α-NaYb(Mn)F_4:Er^{3+}@$NaYF_4$ UCNPs (A) and α-NaYb(Mn)F_4:Tm^{3+}@$NaYF_4$ UCNPs (B) under 980 nm excitation (1 W).

green ratio may be attributed to two factors: one is nonradiative energy transfer between Mn^{2+} and Er^{3+}, the energy transfer from the $^2H_{9/2}$ and $^4S_{3/2}$ state of Er^{3+} to the $^4T_1$ state of Mn^{2+}, followed by back-energy transfer from the $^4T_1$ state of Mn^{2+} to the $^4F_{9/2}$ state of Er^{3+};[46] the other is high concentration of Yb^{3+} in the core, high Yb^{3+} concentration causes the nonradiative energy transfer from the $^4S_{3/2}$ levels of Er^{3+} to the prevalent Yb^{3+}, followed by back-energy transfer to the $^4F_{9/2}$ level of Er^{3+}, thus probably leading to the enhancement of red emission.[50] Figure 3B exhibits the UCL spectrum of α-NaYb(Mn)-F_4:Tm^{3+}@$NaYF_4$ UCNPs under 980 nm irradiation. The emission bands centered at 480, 649, 701, 776, and 803 nm are resolved, and the origin of the UCL bands could be attributed to $^1G_4 \rightarrow {}^3H_6$, $^1G_4 \rightarrow {}^3F_4$, $^3F_{2,3} \rightarrow {}^3H_6$, $^1G_4 \rightarrow {}^3H_5$, and $^3H_4 \rightarrow {}^3H_6$ transitions of Tm^{3+} ions, respectively. It is highly remarkable that two emission bands in the NIR region peaked at 776 and 803 nm are very intense and could be expected to find applications in the biological field where high penetration depth is required.

3.3. Temperature-Dependent Upconversion Luminescence Properties. The α-NaYb(Mn)F_4:Er^{3+}/Tm^{3+}@$NaYF_4$ UCNPs also present fascinating temperature-dependent UCL properties, which enable them to be a promising application as temperature sensors. The temperature-dependent UCL spectra of α-NaYb(Mn)F_4:Er^{3+}@$NaYF_4$ UCNPs ranging from 123 to 423 K are presented in Figure 4. The intensity of 540 and 652 nm emission bands decreases obviously with increasing temperature, while the emission at 522 nm from the $^2H_{11/2}$ level increases slightly (Figures 4B and 4C). These differences could be related to the population redistributions induced by temperature. As to thermal population, it needs the assistance of low-energy phonons to bridge different energy gaps.[51−53]

DOI: 10.1021/acsami.5b05876
ACS Appl. Mater. Interfaces 2015, 7, 20813−20819

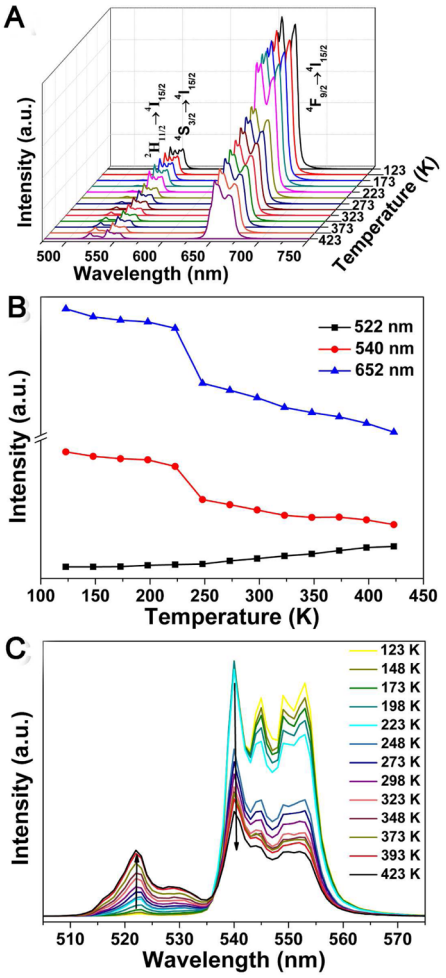

Figure 4. Temperature dependent UCL spectra (A), intensity plots of the emissions at 522, 540, and 652 nm (B), and intensities of the emissions at 522 and 540 nm (C) of α-NaYb(Mn)F_4:Er^{3+}@$NaYF_4$ UCNPs at various temperatures under 980 nm excitation (1 W).

The higher the temperature is, the higher the phonon density is. Higher phonon density not only increases multiphonon relaxations but also favors phonon assisted energy transfer processes. As to the emission bands at 540 and 652 nm, with the increase of temperature, the multiphonon relaxations might be more dominant than the phonon assisted energy transfer processes to repopulate the $^4S_{3/2}$ and $^4F_{9/2}$ states, resulting in the decrease of emission intensity with increasing temperature. To the emission band at 522 nm, however, it should be the other way around. Further studies lead to the discovery that the intensity change rate at temperature below and above 248 K is not identical, and this indicates that the influence of temperature on multiphonon relaxations and phonon assisted energy transfer processes in low and high temperature is different. By contrasting these emission bands, it is discovered that the relative intensity between 522 and 540 nm emission bands makes up "band-shape" luminescence spectra, which refers to a series of spectral lines with different relative intensity (Figure 4C). The intensity ratio R_{Er} of 522 nm ($^2H_{11/2} \rightarrow {}^4I_{15/2}$) and 540 nm ($^4S_{3/2} \rightarrow {}^4I_{15/2}$) increases with temperature rising. The intensity ratio of two emissions makes the temperature sensing independent of the local concentration of the UCNPs and supports for higher thermal sensitivities, thus conquering the main disadvantages of single emission intensity-based measurements. Moreover, the number of photons (Figure S4) involved in the upconversion mechanisms is unchanged at low (173 K), ordinary (298 K), and high temperature (373 K). The knowledge of these variations allows us to verify that $^2H_{11/2}$ and $^4S_{3/2}$ levels are thermally coupled.

The population of thermally coupled levels of active ions follows a Boltzmann-type population distribution, and the ratio R for emission intensity of each thermally coupled level can be expressed as eq 1

$$R = \frac{I_{upper}}{I_{lower}} = A \exp \frac{-\Delta E}{kT} \quad (1)$$

where I_{upper} and I_{lower} are the intensity corresponding to emission bands from the upper and lower levels. A is the proportionality constant, ΔE is the energy gap between two thermally coupled levels $^2H_{11/2}$ and $^4S_{3/2}$, k is the Boltzmann's constant, and T is the absolute temperature.

Figure 5A exhibits the monolog plot of R_{Er} of 522 nm ($^2H_{11/2} \rightarrow {}^4I_{15/2}$) and 540 nm ($^4S_{3/2} \rightarrow {}^4I_{15/2}$) as a function of inverse

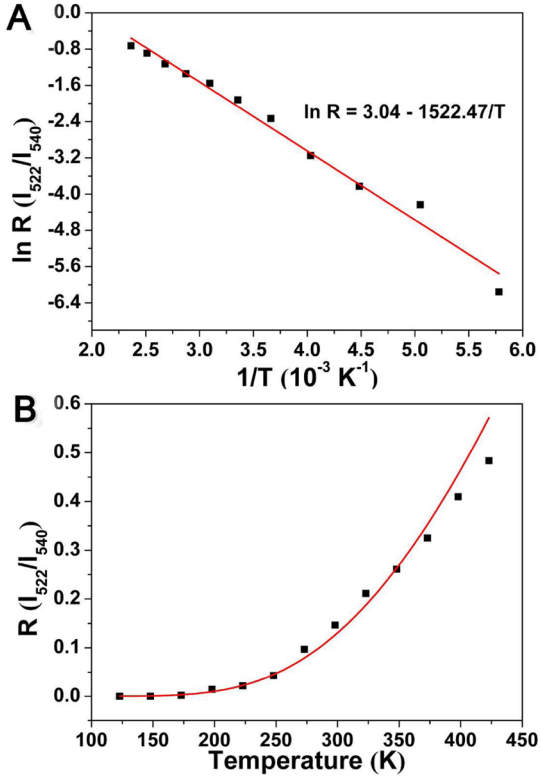

Figure 5. Monolog plot of R_{Er} (I_{522}/I_{540}) as a function of inverse absolute temperature (A) and R_{Er} (I_{522}/I_{540}) as a function of the absolute temperature (B) in the range of 123−423 K under 980 nm excitation (1 W).

absolute temperature, and the linear fitting of the experimental dates obtains the slope value of 1522.47, which gives the $\Delta E/k$ value. ΔE is fitted to be 1058.12 cm^{-1}. R_{Er} is sensitive to the temperature ranging from 123 to 423 K, as shown in Figure 5B, and R_{Er} increases sharply with increasing temperature and agrees well with eq 1. This trend clearly demonstrates that $^2H_{11/2}$ and $^4S_{3/2}$ are suitable thermally coupled levels for the luminescent nanothermometer at this temperature range.[43,54]

Similar results are observed in temperature-dependent UCL spectra of α-NaYb(Mn)F_4:Tm^{3+}@$NaYF_4$ UCNPs at temper-

DOI: 10.1021/acsami.5b05876
ACS Appl. Mater. Interfaces 2015, 7, 20813−20819

ature from 123 to 423 K. As shown in Figure 6, the intensity of all the emission bands decreases with temperature increases,

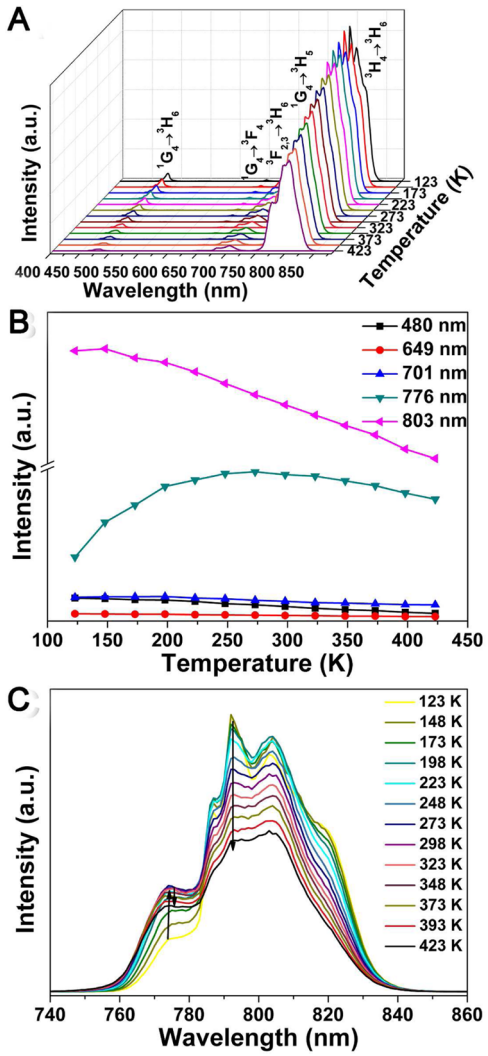

Figure 6. Temperature dependent UCL spectra (A), intensity plots of the emissions at 480, 649, 701, 776, and 803 nm (B), and intensities of the emissions at 776 and 803 nm (C) of α-NaYb(Mn)F_4:Tm^{3+}@$NaYF_4$ UCNPs at various temperatures under 980 nm excitation (1 W).

except for the emission at 776 nm (Figures 6B and 6C), which is found to increase and then decrease with increasing temperature. For the repopulation of the $^1G_4$ states of Tm^{3+} ions below 273 K, phonon assisted energy transfer rates are higher than multiphonon relaxations along with the rise of temperature, thus the intensity of 776 nm emission increases gradually. However, the relative rates quickly turn when the temperature above 273 K lead to the decrease of the emission intensity with the increase of temperature. In spite of this, the variation of the R_{Tm} of 776 nm ($^1G_4 \rightarrow {}^3H_5$) and 803 nm ($^3H_4 \rightarrow {}^3H_6$) as a function of inverse absolute temperature on a monolog scale also displays a linear dependence, as shown in Figure 7A, which gives the slope of about 198.64, and ΔE is 138.05 cm^{-1}, the R_{Tm} related to the absolute temperature between 123 and 423 K also could be fitted to eq 1, and the fitted curve agrees well with the experimental date (Figure 7B). The changing of the intensity ratio in the NIR of Tm^{3+} ($^1G_4 \rightarrow {}^3H_5$ and $^3H_4 \rightarrow {}^3H_6$) with temperature is also observed in

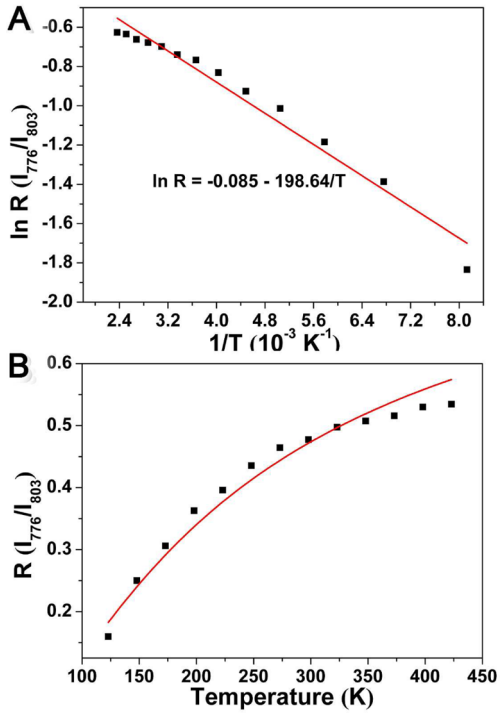

Figure 7. Monolog plot of R_{Tm} (I_{776}/I_{803}) as a function of inverse absolute temperature (A) and R_{Tm} (I_{776}/I_{803}) as a function of the absolute temperature (B) in the range of 123−423 K under 980 nm excitation (1 W).

SrF_2:Tm^{3+},Yb^{3+}. However, it is just the linear fit of the experimental date and does not follow the Boltzmann-type population distribution perfectly.[51]

It is worthwhile to understand the change of sensitivity (S) with temperature, which is defined as the rate of change of R with temperature, and it can be described as eq 2

$$S = \frac{dR}{dT} = R\left(\frac{\Delta E}{kT^2}\right) \quad (2)$$

As shown in Figure 8A, the sensitivity of α-NaYb(Mn)F_4:Er^{3+}@$NaYF_4$ UCNPs increases with the rise of temperature. The maximum sensitivity is noted to be 0.0049 K^{-1} at 423 K. Compared with α-NaYb(Mn)F_4:Er^{3+}@$NaYF_4$ UCNPs, the sensitivity of Tm^{3+}-doped α-NaYb(Mn)F_4@$NaYF_4$ UCNPs (Figure 8B) decreases with increasing temperature, with a maximum value of 0.0024 K^{-1} at 123 K. Although the sensitivity of Er^{3+} or Tm^{3+}-doped α-NaYb(Mn)F_4@$NaYF_4$ UCNPs is not the most optimal, they could make up for each other. That is to say, one could regard Er^{3+} and Tm^{3+}-codoped α-NaYb(Mn)F_4@$NaYF_4$ UCNPs as new luminescent nanothermometers, which show high sensitivity in both low and high temperature range.

4. CONCLUSION

In conclusion, novel flower-like α-NaYb(Mn)F_4@$NaYF_4$ UCNPs have been successfully synthesized by combining liquid−solid solution hydrothermal strategy with thermal decomposition of $Ln(CF_3COO)_3$ precursors. α-NaYb(Mn)F_4:Er^{3+}/Tm^{3+}@$NaYF_4$ UCNPs exhibit intense upconversion luminescence and temperature-dependent UCL performances under 980 nm laser excitation. The temperature-dependent UCL behaviors of Er^{3+} and Tm^{3+} doped α-NaYb(Mn)F_4@$NaYF_4$ UCNPs are as different as they could be due to the

DOI: 10.1021/acsami.5b05876
ACS Appl. Mater. Interfaces 2015, 7, 20813−20819

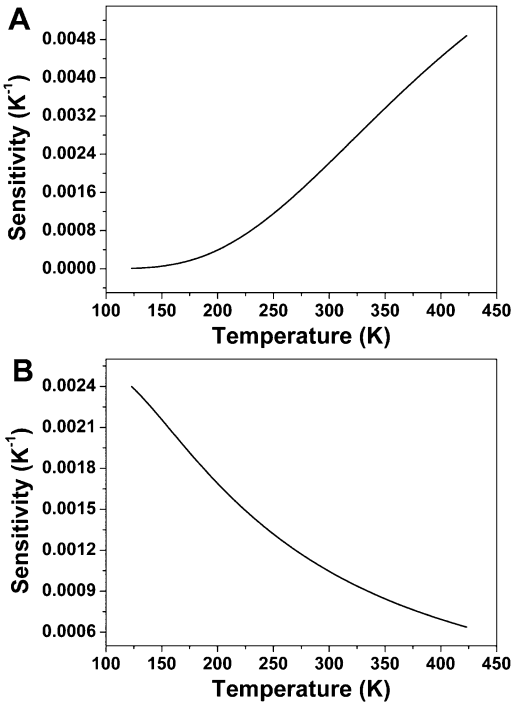

Figure 8. Sensitivity of α-NaYb(Mn)F_4:Er^{3+}@$NaYF_4$ UCNPs (A) and α-NaYb(Mn)F_4:Tm^{3+}@$NaYF_4$ UCNPs (B) as a function of the absolute temperature under 980 nm excitation (1 W).

different phonon density at different temperatures. More importantly, the intensity ratios R_{Er} of $^2H_{11/2} \rightarrow {}^4I_{15/2}$ and $^4S_{3/2} \rightarrow {}^4I_{15/2}$ transitions and R_{Tm} of $^1G_4 \rightarrow {}^3H_5$ and $^3H_4 \rightarrow {}^3H_6$ transitions are sensitive to temperature and agree well with the Boltzmann-type population distribution. The changes in sensitivity of Er^{3+} and Tm^{3+}-doped α-NaYb(Mn)F_4@$NaYF_4$ UCNPs are quite distinct from each other and make up for each other, which enable them to be suitable and excellent candidates for temperature sensing in a wide temperature range with high sensitivity.

■ ASSOCIATED CONTENT

Supporting Information

The Supporting Information is available free of charge on the ACS Publications website at DOI: 10.1021/acsami.5b05876.

Figures S1−S5 (PDF)

■ AUTHOR INFORMATION

Corresponding Authors

*E-mail: fengj@ciac.ac.cn.

*E-mail: hongjie@ciac.ac.cn.

Notes

The authors declare no competing financial interest.

■ ACKNOWLEDGMENTS

The authors are grateful for the financial aid from the National Natural Science Foundation of China (Grant Nos. 21371165, 51372242, 21221061, 91122030, and 21210001), Science and Technology Cooperation Special Project of Hong Kong, Macao, and Taiwan (Grant no. 2014DFT10310), the National Key Basic Research Program of China (No. 2014CB643802), and Jilin Province Youth Foundation (No. 20130522122JH).

■ REFERENCES

(1) Childs, P. R. N.; Greenwood, J. R.; Long, C. A. Review of Temperature Measurement. *Rev. Sci. Instrum.* **2000**, *71*, 2959−2978.

(2) Shakouri, A. Nanoscale Thermal Transport and Microrefrigerators on a Chip. *Proc. IEEE* **2006**, *94*, 1613−1638.

(3) Jundt, D. H. Temperature-Dependent Sellmeier Equation for the Index of Refraction, n_e, in Congruent Lithium Niobate. *Opt. Lett.* **1997**, *22*, 1553−1555.

(4) Jaque, D.; Vetrone, F. Luminescence Nanothermometry. *Nanoscale* **2012**, *4*, 4301−4326.

(5) Wang, X. D.; Wolfbeis, O. S.; Meier, R. J. Luminescent Probes and Sensors for Temperature. *Chem. Soc. Rev.* **2013**, *42*, 7834−7869.

(6) Brites, C. D.; Lima, P. P.; Silva, N. J.; Millan, A.; Amaral, V. S.; Palacio, F.; Carlos, L. D. Thermometry at the Nanoscale. *Nanoscale* **2012**, *4*, 4799−4829.

(7) Vlaskin, V. A.; Janssen, N.; van Rijssel, J.; Beaulac, R.; Gamelin, D. R. Tunable Dual Emission in Doped Semiconductor Nanocrystals. *Nano Lett.* **2010**, *10*, 3670−3674.

(8) McLaurin, E. J.; Vlaskin, V. A.; Gamelin, D. R. Water-Soluble Dual-Emitting Nanocrystals for Ratiometric Optical Thermometry. *J. Am. Chem. Soc.* **2011**, *133*, 14978−14980.

(9) Chandrasekharan, N.; Kelly, L. A. A Dual Fluorescence Temperature Sensor Based on Perylene/Exciplex Interconversion. *J. Am. Chem. Soc.* **2001**, *123*, 9898−9899.

(10) Feng, J.; Tian, K.; Hu, D.; Wang, S.; Li, S.; Zeng, Y.; Li, Y.; Yang, G. A Triarylboron-Based Fluorescent Thermometer: Sensitive Over a Wide Temperature Range. *Angew. Chem., Int. Ed.* **2011**, *50*, 8072−8076.

(11) Zhao, S. N.; Li, L. J.; Song, X. Z.; Zhu, M.; Hao, Z. M.; Meng, X.; Wu, L. L.; Feng, J.; Song, S. Y.; Wang, C. Lanthanide Ion Codoped Emitters for Tailoring Emission Trajectory and Temperature Sensing. *Adv. Funct. Mater.* **2015**, *25*, 1463−1469.

(12) Brites, C. D.; Lima, P. P.; Silva, N. J.; Millan, A.; Amaral, V. S.; Palacio, F.; Carlos, L. D. Lanthanide-Based Luminescent Molecular Thermometers. *New J. Chem.* **2011**, *35*, 1177−1183.

(13) Cadiau, A.; Brites, C. D.; Costa, P. M.; Ferreira, R. A.; Rocha, J.; Carlos, L. D. Ratiometric Nanothermometer Based on an Emissive Ln^{3+}-Organic Framework. *ACS Nano* **2013**, *7*, 7213−7218.

(14) Zheng, S.; Chen, W.; Tan, D.; Zhou, J.; Guo, Q.; Jiang, W.; Xu, C.; Liu, X.; Qiu, J. Lanthanide-Doped $NaGdF_4$ Core−Shell Nanoparticles for Non-Contact Self-Referencing Temperature Sensors. *Nanoscale* **2014**, *6*, 5675−5679.

(15) Yu, J.; Sun, L.; Peng, H.; Stich, M. I. Luminescent Terbium and Europium Probes for Lifetime Based Sensing of Temperature Between 0 and 70 °C. *J. Mater. Chem.* **2010**, *20*, 6975−6981.

(16) Wong, H.-T.; Chan, H. L. W.; Hao, J. Towards Pure Near-Infrared to Near-Infrared Upconversion of Multifunctional GdF_3:Yb^{3+},Tm^{3+} Nanoparticles. *Opt. Express* **2010**, *18*, 6123−6130.

(17) Zhou, J.; Liu, Z.; Li, F. Upconversion Nanophosphors for Small-Animal Imaging. *Chem. Soc. Rev.* **2012**, *41*, 1323−1349.

(18) Auzel, F. Upconversion and Anti-Stokes Processes with f and d Ions in Solids. *Chem. Rev.* **2004**, *104*, 139−173.

(19) Abdul Jalil, R.; Zhang, Y. Biocompatibility of Silica Coated $NaYF_4$ Upconversion Fluorescent Nanocrystals. *Biomaterials* **2008**, *29*, 4122−4128.

(20) Downing, E.; Hesselink, L.; Ralston, J.; Macfarlane, R. A Three-Color, Solid-State, Three-Dimensional Display. *Science* **1996**, *273*, 1185−1189.

(21) Wang, F.; Han, Y.; Lim, C. S.; Lu, Y.; Wang, J.; Xu, J.; Chen, H.; Zhang, C.; Hong, M.; Liu, X. Simultaneous Phase and Size Control of Upconversion Nanocrystals through Lanthanide Doping. *Nature* **2010**, *463*, 1061−1065.

(22) De Wild, J.; Meijerink, A.; Rath, J.; Van Sark, W.; Schropp, R. Towards Upconversion for Amorphous Silicon Solar Cells. *Sol. Energy Mater. Sol. Cells* **2010**, *94*, 1919−1922.

(23) Deng, M. L.; Ma, Y. X.; Huang, S.; Hu, G. F.; Wang, L. Y. Monodisperse Upconversion $NaYF_4$ Nanocrystals: Syntheses and Bioapplications. *Nano Res.* **2011**, *4*, 685−694.

DOI: 10.1021/acsami.5b05876
ACS Appl. Mater. Interfaces 2015, 7, 20813−20819

(24) Xu, S. Y.; Huang, S.; He, Q.; Wang, L. Y. Upconversion Nanophosphores for Bioimaging. *TrAC, Trends Anal. Chem.* **2015**, *66*, 72−79.
(25) Yang, D.; Ma, P.; Hou, Z.; Cheng, Z.; Li, C.; Lin, J. Current Advances in Lanthanide Ion (Ln^{3+})-Based Upconversion Nanomaterials for Drug Delivery. *Chem. Soc. Rev.* **2015**, *44*, 1416−1448.
(26) Idris, N. M.; Jayakumar, M. K. G.; Bansal, A.; Zhang, Y. Upconversion Nanoparticles as Versatile Light Nanotransducers for Photoactivation Applications. *Chem. Soc. Rev.* **2015**, *44*, 1449−1478.
(27) Hou, Y.; Qiao, R.; Fang, F.; Wang, X.; Dong, C.; Liu, K.; Liu, C.; Liu, Z.; Lei, H.; Wang, F.; Gao, M. $NaGdF_4$ Nanoparticle-Based Molecular Probes for Magnetic Resonance Imaging of Intraperitoneal Tumor Xenografts in Vivo. *ACS Nano* **2013**, *7*, 330−338.
(28) Liu, Y.; Ai, K.; Liu, J.; Yuan, Q.; He, Y.; Lu, L. A High-Performance Ytterbium-Based Nanoparticulate Contrast Agent for In Vivo X-ray Computed Tomography Imaging. *Angew. Chem., Int. Ed.* **2012**, *51*, 1437−1442.
(29) Liu, K.; Liu, X.; Zeng, Q.; Zhang, Y.; Tu, L.; Liu, T.; Kong, X.; Wang, Y.; Cao, F.; Lambrechts, S. A. Covalently Assembled NIR Nanoplatform for Simultaneous Fluorescence Imaging and Photodynamic Therapy of Cancer Cells. *ACS Nano* **2012**, *6*, 4054−4062.
(30) Tu, N. N.; Wang, L. Y. Surface Plasmon Resonance Enhanced Upconversion Luminescence in Aqueous Media for TNT Selective Detection. *Chem. Commun.* **2013**, *49*, 6319−6321.
(31) Ma, Y. X.; Huang, S.; Deng, M. L.; Wang, L. Y. White Upconversion Luminescence Nanocrystals for the Simultaneous and Selective Detection of 2,4,6-Trinitrotoluene and 2,4,6-Trinitrophenol. *ACS Appl. Mater. Interfaces* **2014**, *6*, 7790−7796.
(32) Mai, H.-X.; Zhang, Y.-W.; Si, R.; Yan, Z.-G.; Sun, L.-d.; You, L.-P.; Yan, C.-H. High-Quality Sodium Rare-Earth Fluoride Nanocrystals: Controlled Synthesis and Optical Properties. *J. Am. Chem. Soc.* **2006**, *128*, 6426−6436.
(33) Li, X.; Zhang, F.; Zhao, D. Lab on Upconversion Nanoparticles: Optical Properties and Applications Engineering via Designed Nanostructure. *Chem. Soc. Rev.* **2015**, *44*, 1346−1378.
(34) Wang, F.; Liu, X. Recent Advances in the Chemistry of Lanthanide-Doped Upconversion Nanocrystals. *Chem. Soc. Rev.* **2009**, *38*, 976−989.
(35) Sun, X.; Zhang, Y. W.; Du, Y. P.; Yan, Z. G.; Si, R.; You, L. P.; Yan, C. H. From Trifluoroacetate Complex Precursors to Monodisperse Rare-Earth Fluoride and Oxyfluoride Nanocrystals with Diverse Shapes through Controlled Fluorination in Solution Phase. *Chem. - Eur. J.* **2007**, *13*, 2320−2332.
(36) Chen, G.; Ohulchanskyy, T. Y.; Kachynski, A.; Ågren, H.; Prasad, P. N. Intense visible and Near-Infrared Upconversion Photoluminescence in Colloidal $LiYF_4:Er^{3+}$ Nanocrystals under Excitation at 1490 nm. *ACS Nano* **2011**, *5*, 4981−4986.
(37) Deng, M. L.; Wang, L. Y. Unexpected Luminescence Enhancement of Upconverting Nanocrystals by Cation Exchange with well Retained Small Particle Size. *Nano Res.* **2014**, *7*, 782−793.
(38) Fischer, L. H.; Harms, G. S.; Wolfbeis, O. S. Upconverting Nanoparticles for Nanoscale Thermometry. *Angew. Chem., Int. Ed.* **2011**, *50*, 4546−4551.
(39) Sedlmeier, A.; Achatz, D. E.; Fischer, L. H.; Gorris, H. H.; Wolfbeis, O. S. Photon Upconverting Nanoparticles for Luminescent Sensing of Temperature. *Nanoscale* **2012**, *4*, 7090−7096.
(40) Zheng, K.; Liu, Z.; Lv, C.; Qin, W. Temperature Sensor Based on the UV Upconversion Luminescence of Gd^{3+} in Yb^{3+}-Tm^{3+}-Gd^{3+} Codoped $NaLuF_4$ Microcrystals. *J. Mater. Chem. C* **2013**, *1*, 5502−5507.
(41) Vetrone, F.; Naccache, R.; Zamarron, A.; Juarranz de la Fuente, A.; Sanz-Rodríguez, F.; Martinez Maestro, L.; Martín Rodriguez, E.; Jaque, D.; García Solé, J.; Capobianco, J. A. Temperature Sensing Using Fluorescent Nanothermometers. *ACS Nano* **2010**, *4*, 3254−3258.
(42) Dong, N.-N.; Pedroni, M.; Piccinelli, F.; Conti, G.; Sbarbati, A.; Ramírez-Hernández, J. E.; Maestro, L. M.; Iglesias-de la Cruz, M. C.; Sanz-Rodriguez, F.; Juarranz, A. NIR-to-NIR Two-Photon Excited $CaF_2:Tm^{3+},Yb^{3+}$ Nanoparticles: Multifunctional Nanoprobes for Highly Penetrating Fluorescence Bio-Imaging. *ACS Nano* **2011**, *5*, 8665−8671.
(43) Wang, X.; Zheng, J.; Xuan, Y.; Yan, X. Optical Temperature Sensing of $NaYbF_4:Tm^{3+}@SiO_2$ Core-Shell Micro-Particles Induced by Infrared Excitation. *Opt. Express* **2013**, *21*, 21596−21606.
(44) Li, D.; Shao, Q.; Dong, Y.; Jiang, J. Anomalous Temperature-Dependent Upconversion Luminescence of Small-Sized $NaYF_4:Yb^{3+},Er^{3+}$ Nanoparticles. *J. Phys. Chem. C* **2014**, *118*, 22807−22813.
(45) Yu, W.; Xu, W.; Song, H.; Zhang, S. Temperature-Dependent Upconversion Luminescence and Dynamics of $NaYF_4:Yb^{3+}/Er^{3+}$ Nanocrystals: Influence of Particle Size and Crystalline Phase. *Dalton Trans.* **2014**, *43*, 6139−6147.
(46) Tian, G.; Gu, Z.; Zhou, L.; Yin, W.; Liu, X.; Yan, L.; Jin, S.; Ren, W.; Xing, G.; Li, S. Mn^{2+} Dopant-Controlled Synthesis of $NaYF_4$:Yb/Er Upconversion Nanoparticles for in vivo Imaging and Drug Delivery. *Adv. Mater.* **2012**, *24*, 1226−1231.
(47) Roberts, J. E. Lanthanum and Neodymium Salts of Trifluoroacetic Acid. *J. Am. Chem. Soc.* **1961**, *83*, 1087−1088.
(48) Mai, H.-X.; Zhang, Y.-W.; Sun, L.-D.; Yan, C.-H. Highly Efficient Multicolor Up-Conversion Emissions and Their Mechanisms of Monodisperse $NaYF_4$:Yb,Er Core and Core/Shell-Structured Nanocrystals. *J. Phys. Chem. C* **2007**, *111*, 13721−13729.
(49) Johnson, N. J.; van Veggel, F. C. Lanthanide-Based Heteroepitaxial Core-Shell Nanostructures: Compressive versus Tensile Strain Asymmetry. *ACS Nano* **2014**, *8*, 10517−10527.
(50) Punjabi, A.; Wu, X.; Tokatli-Apollon, A.; El-Rifai, M.; Lee, H.; Zhang, Y.; Wang, C.; Liu, Z.; Chan, E. M.; Duan, C. Amplifying the Red-Emission of Upconverting Nanoparticles for Biocompatible Clinically Used Prodrug-Induced Photodynamic Therapy. *ACS Nano* **2014**, *8*, 10621−10630.
(51) Quintanilla, M.; Cantarelli, I. X.; Pedroni, M.; Speghini, A.; Vetrone, F. Intense Ultraviolet Upconversion in Water Dispersible $SrF_2:Tm^{3+},Yb^{3+}$ Nanoparticles: the Effect of the Environment on Light Emissions. *J. Mater. Chem. C* **2015**, *3*, 3108−3113.
(52) Chen, X. Y.; Zhuang, H. Z.; Liu, G. K.; Li, S.; Niedbala, R. S. Confinement on Energy Transfer between Luminescent Centers in Nanocrystals. *J. Appl. Phys.* **2003**, *94*, 5559−5565.
(53) Park, T. R. Phonon-Assisted Energy Up-Conversion Process of Er^{3+} Ions Doped in KYF_4 Crystal. *Solid State Commun.* **2010**, *150*, 1378−1381.
(54) Wade, S. A.; Collins, S. F.; Baxter, G. W. Fluorescence Intensity Ratio Technique for Optical Fiber Point Temperature Sensing. *J. Appl. Phys.* **2003**, *94*, 4743−4756.

DOI: 10.1021/acsami.5b05876
ACS Appl. Mater. Interfaces 2015, 7, 20813−20819